Image reconstruction of effective Mie scattering parameters of breast tissue *in vivo* with near-infrared tomography

Xin Wang
Dartmouth College
Department of Physics and Astronomy
Hanover, New Hampshire 03755

Brian W. Pogue
Shudong Jiang
Hamid Dehghani
Xiaomei Song
Subhadra Srinivasan
Ben A. Brooksby
Keith D. Paulsen
Dartmouth College
Thayer School of Engineering
Hanover, New Hampshire 03755

Christine Kogel
Steven P. Poplack
Dartmouth Medical School
Department of Diagnostic Radiology
Hanover, New Hampshire 03755

Wendy A. Wells
Dartmouth Medical School
Department of Pathology
Hanover, New Hampshire 03755

Abstract. A method for image reconstruction of the effective size and number density of scattering particles is discussed within the context of interpreting near-infrared (NIR) tomography images of breast tissue. An approach to use Mie theory to estimate the effective scattering parameters is examined and applied, given some assumptions about the index of refraction change expected in lipid membrane-bound scatterers. When using a limited number of NIR wavelengths in the reduced scattering spectra, the parameter extraction technique is limited to representing a continuous distribution of scatterer sizes, which is modeled as a simple exponentially decreasing distribution function. In this paper, image formation of effective scatterer size and number density is presented based on the estimation method. The method was evaluated with Intralipid phantom studies to demonstrate particle size estimation to within 9% of the expected value. Then the method was used in NIR patient images, and it indicates that for a cancer tumor, the effective scatterer size is smaller than the background breast values and the effective number density is higher. In contrast, for benign tumor patients, there is not a significant difference in effective scatterer size or number density between tumor and normal tissues. The method was used to interpret magnetic resonance imaging–coupled NIR images of adipose and fibroglandular tissues, and it indicated that the fibroglandular tissue has smaller effective scatterer size and larger effective number density than the adipose tissue does. © *2006 Society of Photo-Optical Instrumentation Engineers.* [DOI: 10.1117/1.2342747]

Keywords: near-infrared; tomography; scattering parameters; mie theory; breast tissue; *in vivo*.

Paper 05290SSRR received Oct. 10, 2005; revised manuscript received Apr. 9, 2006; accepted for publication Apr. 11, 2006; published online Sep. 1, 2006.

1 Introduction

The relationship between the optical and biological properties of tissue is necessary for the optical techniques in tissue diagnostics. Studies have shown that there is excellent contrast in breast lesions relative to normal tissue, and that the scattering contrast between malignant and benign processes appears to be significant.[1] In the past decade, near-infrared (NIR) tomography, which is a method to generate images of internal distributions of optical absorption and scattering at multiple wavelengths by measuring light propagation through tissue, has been developed with considerable interest as a breast imaging modality to characterize abnormalities noninvasively.[2–8] Further, interest exists in exploiting the scattering spectrum of tissue to characterize its microscopic properties, which may provide fundamental insight into the morphological features that are observed in the macroscopic diffuse light signal.[9–16] There have been important advances in particle sizing through Mie scattering theory,[9–13,16–20] which is the model of light scattering for a spherical scatterer with size near the same dimension as the radiation wavelength. In our previous paper,[21] an estimation method was presented to analyze bulk tissue reduced scattering spectra in terms of their effective Mie theory scatterer parameters, effective scatterer size, and number density. In this paper, the image reconstruction method for these effective Mie theory scatterer parameters is presented based on the estimation method in the previous paper.[21]

In estimating effective scatterer size and number density, it is important to focus on what is known and unknown about how light scatters in tissues constituting normal and malignant cells. The morphologic changes from normal to diseased breast tissue are seen by light microscopy in the cellular epithelial component and the surrounding support stroma. Generally, the hallmark of an epithelial malignancy is an increase in the overall epithelial cell density with increased nuclear and nucleolar size. In order to facilitate invasion into the surrounding stroma, subcellular compositional changes in that matrix structure also occur. Microscopic subcellular alter-

Address all correspondence to Brian Pogue, Thayer School of Engineering, Dartmouth College, 8000 Cummings Hall, Hanover, NH 03755; Tel: 603 646-3861; Fax: 603 646-3856; E-mail: pogue@Dartmouth.EDU

ations exist that may not be apparent in standard pathological analysis. Macroscopic scattering of light from tissue is thought to originate from the multiple microscopic fluctuations in refraction index between intracellular organelles and extracellular structures, typically bounded by bilipid membranes.[22–24] Origin of the transport scattering coefficient, which can be measured tomographically is likely to result from these differences in the index of refraction between the extracellular or cytoplasmic fractions of tissue and the lipid composition of the membranes bounding each cell and cellular organelle. Hence, variations in the scattering spectral features, which can be measured tomographically, may encode morphologic and pathophysiologic changes in tissue at the microscopic level. While it is possible to postulate causes of scattering in tissue, it is considerably more difficult to design objective experiments that prove a given hypothesis. Several studies have demonstrated that light transport in tissue is dominated by elastic scattering. The applicability of Mie theory is only approximate because it strictly applies only for spheres in a homogeneous background,[25,26] yet such approximations have been used successfully in the interpretation of natural scattering phenomenon and are explained here as a reasonable first order approximate.[27]

Most of the previous studies of scatterer size determination from scattering spectra have been focused on mucosal diseases or dilute cell suspensions where the scattering by cell nuclei has been a primary emphasis,[9–16] and in general, an increased nuclear scatterer size has been found in the diseased tissue. In these studies, subtle oscillations in the scattering spectrum were used to estimate nuclear size through fits to Mie calculations. In other investigations, more focus has been paid to the scattering of small particles in tissue. However, the extent to which small and large particle size scatterers can be simultaneously fit with sparse data is not yet clear, although with full angular or spectral reflectance, it is evident that reasonable estimation of both can be achieved.[28–31] Mie scattering interpretation serves as a reasonable starting point to analyze elastic transport scattering spectra, and with sparse wavelength data, it appears likely that only information about smaller scattering particles can be effectively estimated.

In prior attempts to estimate effective scatterer size, assumptions about the histogram of scatterer sizes in tissue were made to reduce the estimation problem to be a two-parameter (average scatterer size and number density, which are called as the effective scatterer size and number density) estimation problem. For larger particles, like cell nuclei, the histogram shape has been assumed to be Gaussian.[11,29,32–34] However, smaller particles, like mitochondria, Golgi bodies, lysosomes, and such, have often been assumed to be arranged in a log-normal distribution.[10] There is also a strong rationale for using a simple exponential function for the distribution of smaller particles in tissue, as the density of smaller organelle structures clearly continues to decrease well below our ability to image these structures with optical microscopy. In tissue phantom studies, Intralipid provides a distribution of sizes where the histogram has been determined by electron microscopy to be exponentially distributed[25] with an average size of 97 nm. In this paper, an exponential distribution of scattering particle sizes is used to interpret the scattering spectra of both Intralipid phantom and human breast tissue.

One of the goals of NIR tomography research has been to provide clinicians with new information about the underlying properties of benign and malignant breast disease.[8,35–38] However, there is emerging data indicating that NIR scattering spectra are correlated to the normal composition of breast tissue and that changes in breast physiology can be detected by variations in scattering spectra.[39,40]

In a previous paper,[21] the method for extracting effective scatterer size and number density from the reduced scattering coefficient spectrum was proposed. The scattering spectrum was sampled at 6 wavelengths (661, 761, 785, 808, 826, and 849 nm) measured for transmission through normal breast tissue using a clinical breast tomography system. In this paper, the image reconstruction method for the effective Mie theory scattering parameters is proposed based on the estimation method in the previous paper. The assumptions and limitations of this image reconstruction process are discussed to put the study in perspective with prior work, and the method utilized is analyzed through simulated and tissue-phantom data to establish its accuracy. The value of image reconstruction for effective scatterer size and number density from tomography data could be quite significant; hence, methods to further test and implement the approach are discussed. Acceptance of the relevance of particle size and number density could be easier than the more abstract quantities of scattering amplitude and power, thus this work could have important benefits in the field of medical use of diffuse tomography.

2 Methods

2.1 Mie Scattering Theory Interpretation

Mie theory[26] provides an exact solution for elastic scatter, in the case of a perfect dielectric sphere of arbitrary size in a uniform background medium. Using Mie theory, the reduced scattering coefficient spectra of bulk homogeneous samples can also be expressed quantitatively, with the homogeneous medium equation as

$$\mu_s'(\lambda) = N(\pi a^2) Q_{scat}(m,a,\lambda)[1 - g(m,a,\lambda)], \qquad (1)$$

where λ is the wavelength, N is the number density of the scatterer, a is the scatterer size (the diameter of the scattering particle), m is the relative refractive index ($m = n_2/n_1$, where n_1 and n_2 are the refractive index outside and inside the particles, respectively) and $Q_{scat}(m,a,\lambda)$ is a dimensionless scattering efficiency factor that is calculated from an analytic series expansion that is the solution to the scattered wave intensity from the sphere. Mie theory can be extended to approximate a multisized scattering particle medium by simply summing the scattering contributions over all scattering particle sizes and adding an approximate normalized size distribution factor, $f(a)$, which describes the histogram of scattering particle number density per unit particle size, in which case Eq. (1) becomes

$$\mu_s'(\lambda) = N \sum_{i=1}^{p} f(a_i)(\pi a_i^2) Q_{scat}(m,a,\lambda)[1 - g(m,a,\lambda)]. \quad (2)$$

The average scatterer size could be expressed as

$$\langle a \rangle = \sum_i a_i f(a_i). \qquad (3)$$

Equation (2) has implicit assumptions that the scattering particle index changes are all the same, which is a limitation that should be recalled when it is applied in various problems. However, the simulation study resuls in an earlier paper[21] indicated that the index changes typically result only in changes of amplitude in μ_s', rather than changes in the spectral features in the NIR regime. Thus, while the assumption of constant m is unfortunate, it still does allow an estimation of the scattering particle size, given some *a priori* information about the $f(a_i)$ function.

A more empirical approach to Mie theory was first proposed by van Staveren et al.[25] in fitting the scattering spectrum of Intralipid. A number of groups have adopted the approach to characterize the spectrum of the reduced scattering coefficient observed in tissues.[37,40–42] In these studies, the scattering spectra are considered to satisfy a power law relationship, similar to Rayleigh scattering where the scatter coefficient decreases as λ^{-4}, but using a power value smaller than 4. Empirically, when there is a broad range of scattering particle sizes, this spectrum is described by a power law curve of the type

$$\mu_s'(\lambda) = A\lambda^{-b}, \qquad (4)$$

where A and b are model parameters for scattering amplitude and scattering power, respectively. Equation (4) describes a smooth function with no oscillations in the spectrum and conveniently restricts the fitting process to only two parameters. The curve is quasi-linear in the NIR region and appears to fit data from a large number of wavelengths reasonably well.[43]

2.2 Scattering from Tissue Spectra

In Eq. (2), the number density only influences the amplitude of the scattering spectra in the NIR range, and there are only two parameters to determine the shape of the scattering spectra including (i) the distribution function and (ii) the relative refractive index. The distribution function could be separated into two parts: the type of the distribution function and the average size. So there are three parameters to determine the shape of the scattering spectra including (i) the type of the distribution function, (ii) the average scatterer size, $\langle a \rangle$, and (iii) the relative refractive index. If the type of the distribution function and relative refractive index can be set by some known information, then there are only two parameters left to estimate in Eq. (2): average scatterer size and number density,[21] which are called the effective scatterer size and number density. Considering that the effective scatterer size influences the shape of the scattering spectra in these two parameters, the effective scatterer size can be estimated by comparing the shape of the scattering spectra obtained with Mie theory. Then, using this effective scatterer size estimate, the effective number density can be calculated by comparing the magnitude of the scattering spectra with Mie theory.

2.3 Image Reconstruction of Absorption and Scattering Coefficients

Reduced scattering coefficients were obtained with the clinical imaging system in use at Dartmouth (see Ref. 44 for de-

tails). Briefly, the system measures diffusely transmitted amplitude and phase shift at 100 MHz through up to 12 cm of tissue and is designed for breast imaging for characterization of tumors noninvasively. The measurements are taken at six wavelengths (661, 761, 785, 808, 826, and 849 nm), the data is calibrated by a homogeneous phantom, and then fit to a finite element diffusion theory prediction of the data. The finite element model is iteratively fit to the measurements through a Newton minimization method, and images of absorption and reduced scattering coefficient are recovered at all wavelengths. In recent years, a direct reconstruction approach has been implemented that uses the known spectrum of the absorbing species in the tissue (hemoglobin, oxyhemoglobin, water) and the assumed model of scattering shown in Eq. (4). This inversion algorithm is described in detail in previous papers and is believed to provide more accurate prediction of the scattering parameters A and b from Eq. (4).[45,46] However, related to the fitting for particle size and density, it must be clearly understood that a sparse number of wavelengths cannot be used to accurately fit a highly detailed scattering spectrum, and in fact, oscillations in the spectrum have not been observed to date in bulk tissues. Thus the limited number of wavelengths is not sufficient for identifying oscillations in the scattering spectra that might be observed from larger Mie scattering particles, and these have not been observed with any certainty in diffuse spectra. However, oscillation in the diffuse spectra can be omitted if the dominant scattering particle sizes are thought to be smaller than 1000 nm.[21]

2.4 Effective Scatterer Size and Number Density Estimation Method

To estimate effective scatterer size and number density, with the limited number of wavelengths available, any oscillation in the spectra must be omitted because the dominant scatterer sizes expected are small. The six experimental reduced scattering coefficients are fit to predictions of the power law expression in Eq. (4), first to get the scattering amplitude and scattering power, and then to generate a function of reduced scattering coefficient as a function of wavelength from 650 to 1000 nm. To extract the average particle size, this reduced scattering coefficient function is normalized at one wavelength (800 nm). This normalization eliminates the influence of number density, so that only average particle size needs to be fit in the first stage. Using a least-squares minimization, the average particle size can be effectively estimated. Then the number density can then be estimated by comparing the original unnormalized data with Mie theory [Eq. (2)] using a second least-squares minimization method. In this fitting, the following error function is used:

$$\chi = \left\{ \frac{1}{n} \sum_{i=1}^{n} [(\mu_s'^i \exp - \mu_s'^i o)/\mu_s'^i o]^2 \right\}^{1/2}, \qquad (5)$$

where χ is the error norm, n is the total number of wavelengths used in the fitting process, $\mu_s^{i}{}' \exp$ is the experimental reduced scattering coefficient at the i*th* wavelength, $\mu_s^{i}{}' o$ is the reduced scattering coefficient at the i*th* wavelength calculated from Mie theory. Further details of this estimation method are provided in an earlier paper.[21]

Table 1 Power function estimates for effective scatterer size $\langle a \rangle$ and normalized number density N_0, given the index of refraction values specified for outside (n_1) and inside (n_2) the spheres. For $\langle a \rangle$, the power series was taken out to seven orders, whereas for N_0 only three orders were required.

Power order	Bilipid membrane $n_1 = 1.36,\ n_2 = 1.4$		Adipose tissue $n_1 = 1.36,\ n_2 = 1.49$		Intralipid phantom $n_1 = 1.33,\ n_2 = 1.47$	
	$\langle a \rangle$ (nm)	N_0 (m^{-3})	$\langle a \rangle$ (nm)	N_0 (m^{-3})	$\langle a \rangle$ (nm)	N_0 (m^{-3})
0	2.93×10^3	14.7	3.1×10^3	14.0	6.67×10^3	13.5
1	-9.57×10^3	3.76	-1.09×10^4	2.87	-2.67×10^4	3.41
2	1.35×10^4	-2.71	1.67×10^4	-2.18	4.43×10^4	-2.42
3	-1.03×10^4	0.403	-1.38×10^4	0.316	3.89×10^4	0.35
4	4.52×10^3		6.58×10^3		1.94×10^4	
5	-1.15×10^3		-1.81×10^3		-5.55×10^3	
6	1.58×10^2		2.68×10^2		8.45×10^2	
7	-8.96		-16.4		-53.1	

2.5 Effective Scatterer Size and Number Density Image Reconstruction Method

From the estimation method briefly presented above, the effective scatterer size, $\langle a \rangle$, and number density, N, images are estimated from experimental measurements of the scattering power b and amplitude A. Data in Ref. 21 showed that out of $\langle a \rangle$ and N, it is only $\langle a \rangle$ that influences the shape of the scattering spectra in the NIR region. Effective scatterer size $\langle a \rangle$ can therefore be directly estimated from the experimental value of b. When the scattering amplitude is normalized to $A = 1$ at 800 nm, the effective number density $N = N_0$ is also, such that N_0 is also determined only by the scattering power b. Then for arbitrary A, the effective number density can then be estimated by $N = AN_0$. So given A and b, both $\langle a \rangle$ and N can be estimated with this sequential process.

By simulating a series of b values to get the results for $\langle a \rangle$ and N_0, an empirical polynomial power function was found for $\langle a \rangle$ as a function of b, and for N_0 as a function of b. The equations for $\langle a \rangle$ and N_0 are represented as polynomial expressions, listed in Table 1. The fit to the data for $\langle a \rangle$ was found to be optimal with a seventh order polynomial, whereas the fit to the data for N_0 required only a third order polynomial.

2.6 Phantom Study

Data from the tomography system was used to validate this estimation approach by initially using tissue-simulating phantoms with well-characterized particle size and density. Heterogeneous gelatin phantoms were used, containing Intralipid inclusions at five different concentrations, ranging from 0.75 to 1.75% in steps of 0.25%. This range of inclusion concentrations provided a reduced scattering coefficient spectrum with the same particle size but linearly increasing number density. The data at each concentration was analyzed with the method described above with image reconstruction for the effective scatterer size and number density. By varying the concentration, each spectrum is expected to result in the same $\langle a \rangle$, with a theoretical value near 97($\pm$3) nm, as measured by van Staveren et al.[25] This experiment provided an effective way to examine imaging inclusions within an otherwise homogeneous domain.

2.7 Image Reconstruction of $\langle a \rangle$ and N for Human Breast Tissue

In the second step, the image reconstruction method was applied to cancer breast tissue images. The study was approved by the institutional committee for the protection of human subjects. NIR imaging studies were performed on symptomatic women recruited into the study following an abnormal mammogram and at the time of referral to biopsy. Informed consent was provided prior to the NIR imaging exam. Data from 12 patients were used in the analysis presented here, including 3 cancer patients and 9 benign tumor patients. For the diseased breast, both the cancer tissue and the background normal tissue were studied; the region of the tumor was delineated manually based upon a radiologist's prediction of the location of the lesion from the x-ray mammograms. The regional average value was calculated for both the tumor and the normal tissue values. The contralateral breast was also analyzed separately as a whole value. Reconstruction of images for all patients was done with a direct estimate of the scattering parameters based upon an algorithm that incorporates all six wavelength data sets simultaneously and constrains the fitted images to recover hemoglobin, oxygen saturation, water fraction, and scattering spectra, fitted to A and b parameters.

2.8 Study of Subject Images from the MRI-NIR System

In a final stage in the testing of the parameter estimation approach, the data processing method was applied to images

from a magnetic resonance imaging (MRI)-coupled NIR system for breast tissue imaging. A clinical prototype hybrid imaging system, which combines NIR spectral tomography and MRI, was used to determine tissue structure with improved spatial resolution.[47–50] Combining these two methodologies into a platform for simultaneous data acquisition allowed for excellent coregistration and data synergy. NIR reconstructions that use appropriate spatial constraints from *a priori* structural information about the boundary between adipose and fibroglandular tissue, lead to images with millimeter resolution and better represent the physiological differences between these two types of tissue. Thus, these images were used with the algorithm to predict effective scatterer size and number density to examine the typical values for adipose and fibroglandular tissue.

The imaging system used, described in detail by Brooksby et al.,[48] records measurements of NIR light transmission through a pendant breast in a planar, tomographic geometry. A portable cart houses the light generation and detection hardware subsystems. Six laser diodes (660 to 850 nm) are amplitude modulated at 100 MHz. The bank of laser tubes is mounted on a linear translation stage, which sequentially couples the activated source into 16 bifurcated optical fiber bundles. The central seven fibers deliver the source light while the remaining fibers collect transmitted light and are coupled to photomultiplier tube (PMT) detectors located in the base of the cart. For each source, measurements of the amplitude and phase shift of the 100 MHz signal are acquired from 15 locations around the breast. The optical fiber bundles extend 13 m into a 1.5 T whole body MRI (GE Medical Systems), and the two data types (i.e., NIR and MRI) are acquired simultaneously. The patient lies on an open architecture breast array coil (MRI Devices) that also houses the MRI-compatible fiber positioning system. The plane of fibers spanning the circumference of a pendant breast can be positioned manually from nipple to chest wall if multiple planes of NIR data are desired.

Experience has shown that significant improvement in the stability and accuracy of the reconstruction process can be obtained by incorporating prior anatomical information as an input in the NIR parameter estimation problem.[48,50–59] MRI priors are implemented through the incorporation of a regularization matrix, which has a Laplacian filter shape within the same tissue type, and effectively relaxes these smoothness constraints at the interface between different tissues, in directions normal to their common boundary.[50] This approach provides an inherent smoothing of a given tissue type, such as adipose or glandular tissues, but allows the two tissue types to be significantly different from one another. Based upon a series of phantom studies, this approach, combined with direct spectral reconstruction, has been shown to be the best estimate of the chromophore concentrations and scattering parameters of these normal breast tissues. The values of A and b in these images were then used to generate images of effective scatterer size and number density.

3 Results

3.1 Empirical Equations for Estimation of $\langle a \rangle$ and N

In the imaging problem, the use of the empirical power functions listed in Table 1 were ideal to map the reconstructed
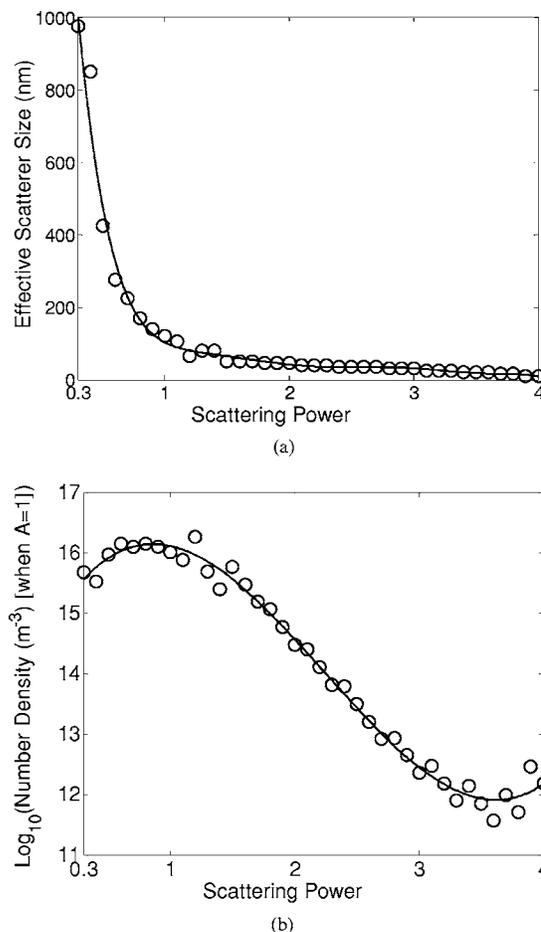

Fig. 1 The relationship between scatter power, b, and effective scatterer size, $\langle a \rangle$, is shown in (a) for simulated data (points) and the best fit polynomial curve (coefficients in Table 1). The relationship between effective normalized number density (the effective number density when $A=1$) and scatter power is shown in (b) for the same parameters, with the fitted polynomial curve shown (coefficients in Table 1).

images of scattering parameters onto the effective scatterer size and number density images. In all these studies, the size distribution function was assumed to be an exponentially decreasing function, and their corresponding relative refractive indexes were used. For the phantom study, $n_1 = 1.33$, $n_2 = 1.47$ were used,[25] and for the cancer patient study, $n_1 = 1.36$, $n_2 = 1.4$ were used.[22] For the MRI-NIR patient studies, where the tissues could be uniquely segmented between adipose and fibroglandular tissues, $n_1 = 1.36$ and $n_2 = 1.4$ were used for the fibroglandular tissue, with the latter value being taken for bilipid membranes,[22] while for the adipose tissues, $n_1 = 1.36$ and $n_2 = 1.49$ were used with the latter value being the measured value for the lipid.[50] The corresponding empirical equations for these three sets of refractive indexes were estimated and the coefficients are shown in Table 1. The fitting figures for the $n_1 = 1.36$, $n_2 = 1.4$ set are shown in Fig. 1.

3.2 Phantom Study Results

Figure 2(a) shows the diagram of the phantom, and 2(b) shows the reconstructed images for b (Scatt. Power) and A
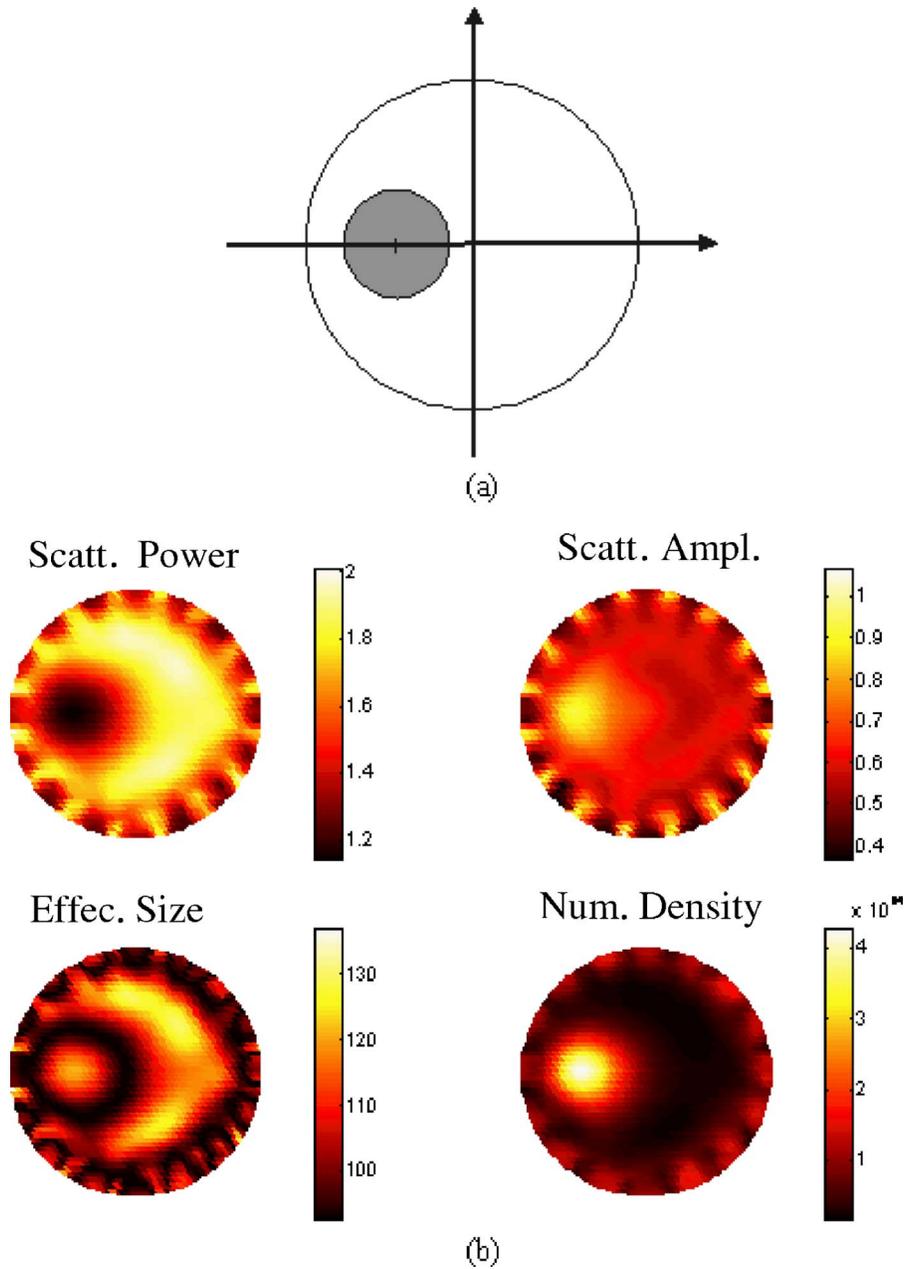
Fig. 2 In (a), a diagram of the phantom geometry is shown, and in (b), a set of reconstructed images of the phantom with 1.0% Intralipid concentration is shown. The background medium was a solid resin phantom used in many previous studies (Refs. 46 and 62).

(Scatt. Ampl.), from the phantom with an inclusion of In-tralipid at concentration of 1.0%. From these two images and using the empirical equations, the reconstructed images of effective scatterer size (Effec. Size) and number density (Num. Density) were obtained as shown in 2(b).

The physical region of interest (ROI) was taken as the size of the hole, and the average value over the ROI was esti-mated. For example, for the phantom with an Intralipid con-centration of 1.0% in the inclusion, the effective scatterer size and number density average values in the ROI were 111 nm and 2.64×10^{14} m^{-3}.

The summary values for each of the five phantom concen-trations of Intralipid is shown in Fig. 3, with 3(a) showing the

effective scatterer size. The circles indicate the results for the phantom data. The estimation results for the phantoms with different intralipid concentrations were almost all the same, with an average value of 106 nm, which is shown by the solid line in Fig. 3(a), and standard deviation was 4 nm. This result agrees to within 9% of the expected value of 97 ± 3 nm from van Staveren et al., as determined by electron microscopy studies in their paper.[25]

Figure 3(b) shows the result for the ratio of effective num-ber density to concentration, for varying concentrations of the Intralipid inclusion. The circles indicate the results, with the ratio of N over concentration being nearly constant for these
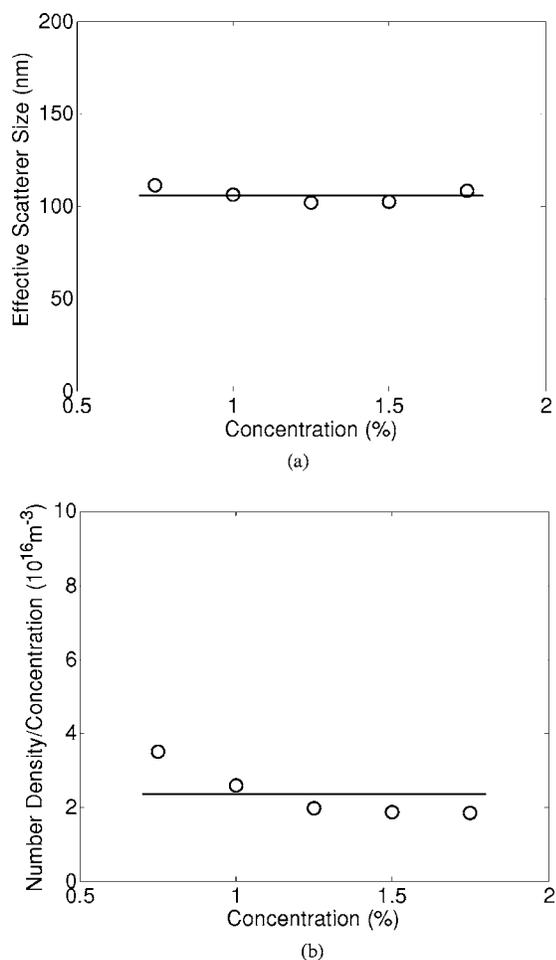
(a)

(b)

Fig. 3 The results are shown for different intralipid concentrations of (a) average effective scatterer size, $\langle a \rangle$, and (b) average effective number density, N, using bulk values from within the inclusion region, as shown in Fig. 2.

phantoms, having average and standard deviation values of 2.4×10^{16} m^{-3} $\pm 0.7 \times 10^{16}$ m^{-3}, which are shown by the solid line in Fig. 3(b). Because these phantom results were consistent with what was expected, the approach was utilized on human data, which is discussed in Sec. 3.3.

3.3 Patient Imaging Study Results

Figure 4(a) is a representative image example from a patient with an invasive ductal carcinoma tumor in the breast, showing an en face or craniocaudal slice of the breast as viewed toward the patient. From our reconstruction, the hemoglobin (Hb$_T$), oxygen saturation (Oxy.), water fraction (Wat.), scattering power (Scatt. Power), and scattering amplitude (Scatt. Ampl.) images were recovered, and these are all shown in Fig. 4(a) in the plane of the tumor. Using the two empirical equations for $n_1 = 1.36$, $n_2 = 1.4$, the effective scatterer size and number density values were recovered at each pixel in the image, using the images of the scattering power and scattering amplitude. The resulting images are also shown in Fig. 4(a). These images indicate that the cancer tissue has smaller effective scatterer size and larger effective number density than the

background in this case. Figure 4(b) is a representative image example from a patient with a benign tumor in the breast.
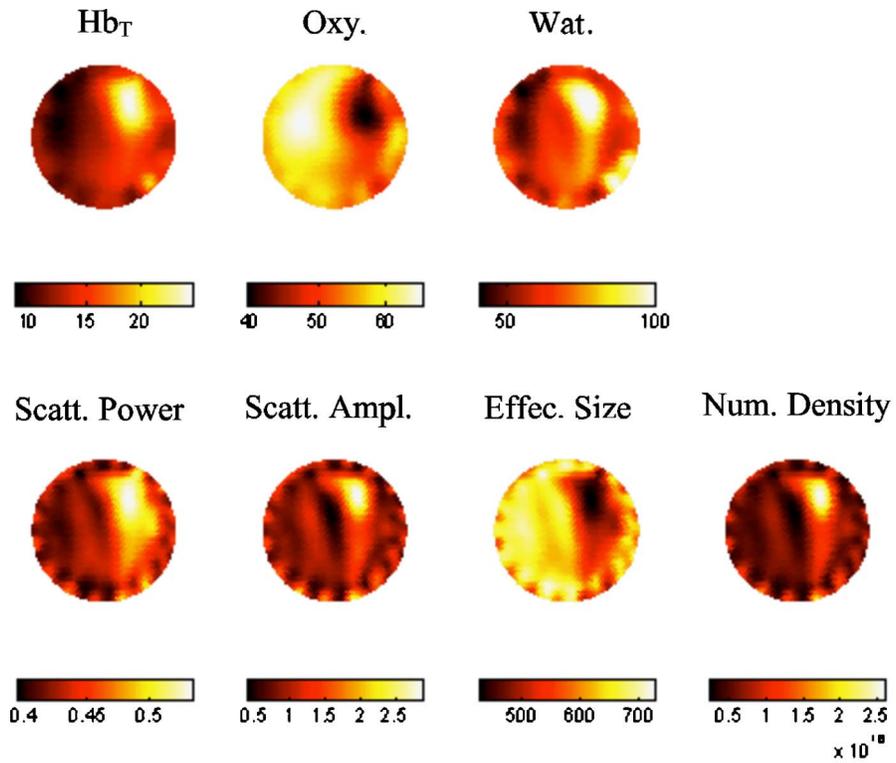
The ROI value is the average over the tumor area. The average value over the remaining breast tissue excluded the tumor ROI. The average value for the contralateral breast ROI was estimated at the same mirror location as in the symptomatic breast. Studies have shown that breast tissue is highly symmetric between breasts, such that comparisons between ROI values taken from mirror locations in the symptomatic and normal breasts are a good way to see differences from the normal condition.

Figure 5 is the summary data for the patients, including the cancer patients and the benign tumor patients. Figures 5(a) and 5(b) show the average effective scatterer size and number density values for the ROI, the background and contralateral breast over all the cancer patients included in this study, as well as the benign tumor patients. For the average effective scatterer size in the ROI, the *t*-test value between of the cancer patients and the benign patients is 0.025. The data in Figs. 5(a) and 5(b) indicate that for the cancer patients, the ROI has smaller effective scatterer size and larger effective number density compared with both the background and the contralateral breast; while for the benign tumors, effective scatterer size and number density are all relatively close to that of the background and the contralateral breast values. But it needs to be mentioned that there are too few cancer patients to obtain a generic conclusion about tumors in this study. More patients will be studied in the future to reach such a conclusion. Figures 6(a) and 6(b) show the average difference over each kind of patient for effective scatterer size $\langle a \rangle$ and number density N between the ROI and background and between the ROI and the contralateral breast.
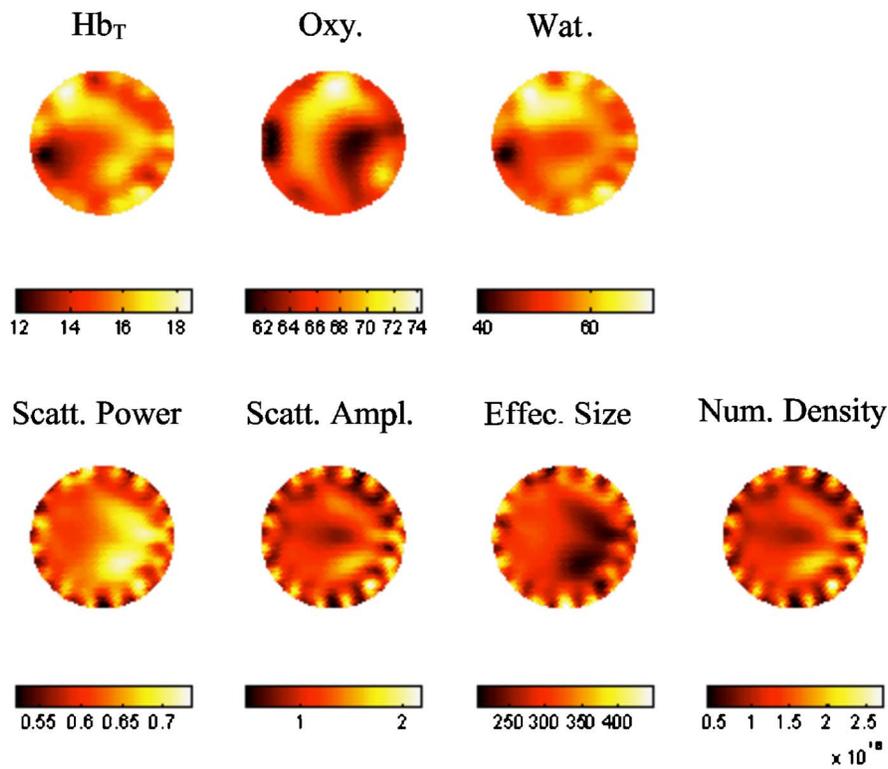
3.4 MRI-NIR Subject Study Results

In the final stage of examining the predictions for effective scatterer size and number density values, the images reconstructed with combined MRI-NIR were used.[62] The results for two MRI-NIR patients are shown in Figs. 7(a) and 7(b). Figure 7(a) (Region) is the MRI image for the first patient. The inner part of the breast (darker in the image) is the fibroglandular tissue, and the outer part (gray in color) is the adipose or fatty tissue. The hemoglobin (Hb$_T$), oxygen saturation (Oxy.), water fraction (Wat.), and scattering power (Scatt. Power) and amplitude (Scatt. Ampl.) images are shown in Fig. 7(a). In the estimation of $\langle a \rangle$ and N images, separate values for n_2 were used for each of the two tissue types, as discussed in Sec. 2, and images of the breast interior were recovered. The estimated images for $\langle a \rangle$ (Effec. Size) and N (Num. Density) are also shown in Fig. 7(a). These images indicate that the fibroglandular tissue has smaller effective scatterer size and larger effective number density than the fatty tissue. For the second patient, the same conclusion is obtained from these results.

In total, 10 sets of images from the MRI-NIR subjects were used in this evaluation and the summary result for these is shown in Fig. 8. The summary results show that the fibroglandular tissue has smaller effective scatterer size and larger effective number density than the adipose tissue. For the average effective scatterer size, the *t* test between of the fibroglandular and adipose tissue showed a significant difference with a *p* value of 0.048. For the number density, the *t* test

Fig. 4 In (a), reconstructed NIR images are shown for a cancer patient, showing the plane of the tumor in the breast, sliced in a craniocaudal view. The panel of images shows total hemoglobin concentration (Hb_T), oxygen saturation (Oxy.), water fraction (Wat.), scatter power (Scatt. Power) and amplitude (Scatt. Ampl.), as well as effective scatterer size (Effec. Size), and number density (Num. Density) images. In (b), the reconstructed NIR images for a patient with a benign tumor in the breast are shown.

(a)

(b)

Fig. 5 The values for groups of subjects in terms of cancer and benign lesions are shown, for (a) average effective scatterer sizes and (b) average effective number density.

(a)

(b)

Fig. 6 The relative differences in average region values are shown for cancer and benign lesions for (a) average effective scatterer sizes and (b) average effective number density.

showed a significant difference between the fibroglandular and adipose tissue with a smaller p value of 0.004. Thus NIR tomography appears to be able to delineate fibroglandular tissue from fatty tissue more by the number density than by the average size.

4 Discussion

Overall, results in this paper indicate that by defining the scattering particle size and density distribution functions and assuming values of refractive indexes, Mie theory could be used to estimate images of bulk effective scatterer size and number density. The estimates have been derived from bulk transport scattering measurements at six discrete wavelengths, 661, 761, 785, 808, 826, and 849 nm, assuming the reduced scattering spectrum is smooth in shape across the wavelength range. The inherent assumptions in this approach are that the scattering particle size histogram of values is exponentially weighted to smaller size particles and that the index of refraction can be expressed as a single pair of values inside and outside of the particles. As shown in a previous paper,[21] smaller particle sizes lead to similar reduced transport scattering spectra with little oscillation, whereas particles above 1 μm in size generate visible oscillations in the reduced scattering spectra as a function of wavelength. Thus, any smoothness assumption in scattering spectrum inherently limits the results to estimating smaller scatterer sizes. The scattering spectra currently reported for bulk breast tissue do not show a
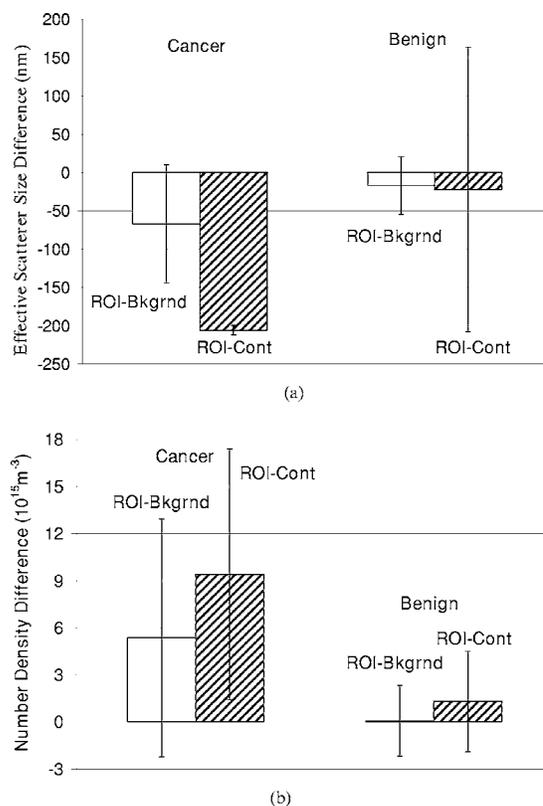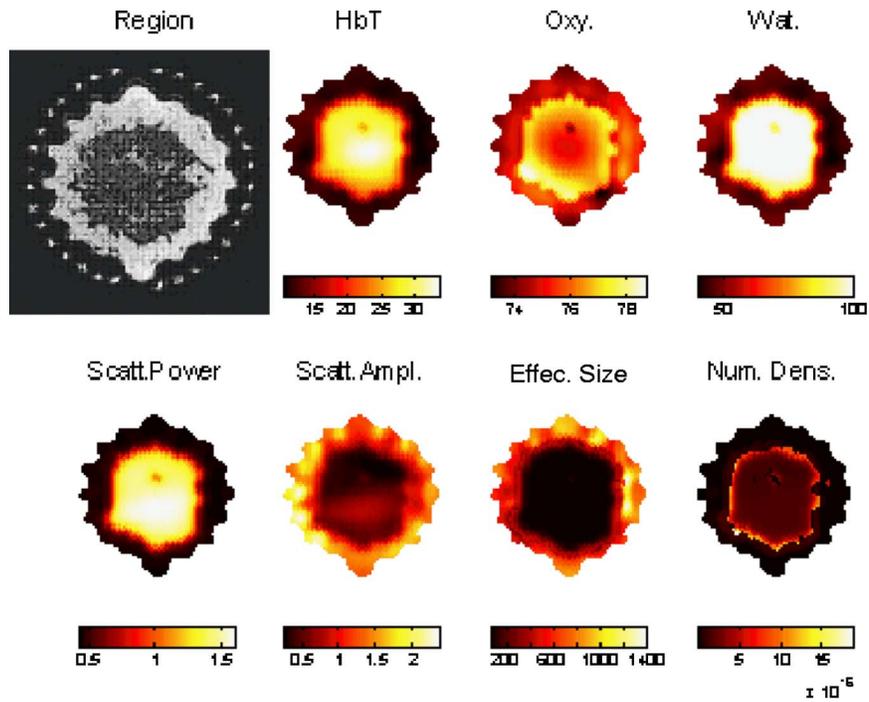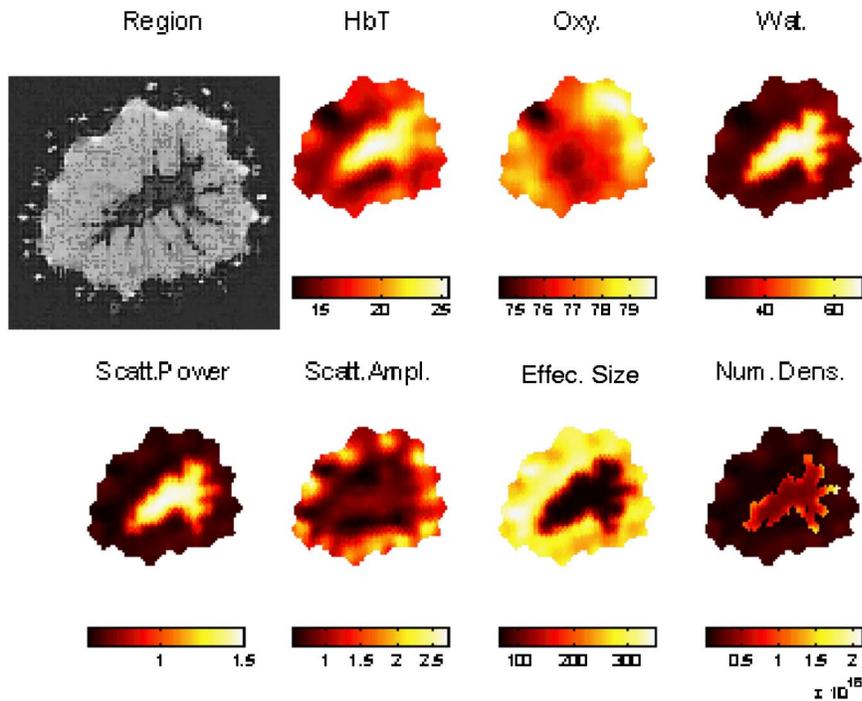
significant presence of oscillations as a function of wavelength.[6,41,43,60,61] While this observation could be an artifact of the data processing, it is also reasonable to assume that the dominant scattering particle sizes are less than 1 μm. When imaging cells with phase contrast microscopy, the total backscatter due to the cytoplasm is typically much more significant than the nucleus, indicating that intracellular structures other than the nucleus are important determinants of the scattering spectra, leading to larger fractional oscillations in the spectrum recovered.

In this work, it was assumed that the distribution of scattering particle sizes is exponentially weighted to smaller values. The rationale for this comes from the observation that the largest number of membrane-bound structures in tissue are considerably smaller than the nucleus. So although larger structures, such as cell nuclei, typically 5 to 15 μm in diameter, are known to scatter light, the primary small scattering centers in tissue are thought to be the collagen fiber network of the extracellular matrix, the mitochondria, and other intracellular entities with dimensions smaller than the optical wavelengths.[25] Nonetheless, this assumption is an unsatisfactory compromise, but one that is routinely employed in elastic scattering spectroscopy, and should be further studied. Yet given the difficulties in extracting subwavelength information from samples, it is likely a problem without an easy solution at this time in point.

Given these assumptions and limitations, a fitting procedure is possible where the normalized scattering spectra are

(a)

(b)

Fig. 7 Reconstructed images for two of the MRI-NIR subjects (a,b) are shown, with the MRI image in (Region), and hemoglobin (Hb$_T$), oxygen saturation (Oxy.), water fraction (Wat.), scatter power (Scatt. Power), and scatter amplitude (Scatt. Ampl.). Estimates of $\langle a \rangle$ and N are shown in (Effec. Size) and (Num. Dens.), as calculated from (Scatt. Power) and (Scatt. Ampl.). Image (b) is predominantly fatty tissue (gray in MRI image), whereas (a) is predominantly fibroglandular tissue (darker in MRI image).
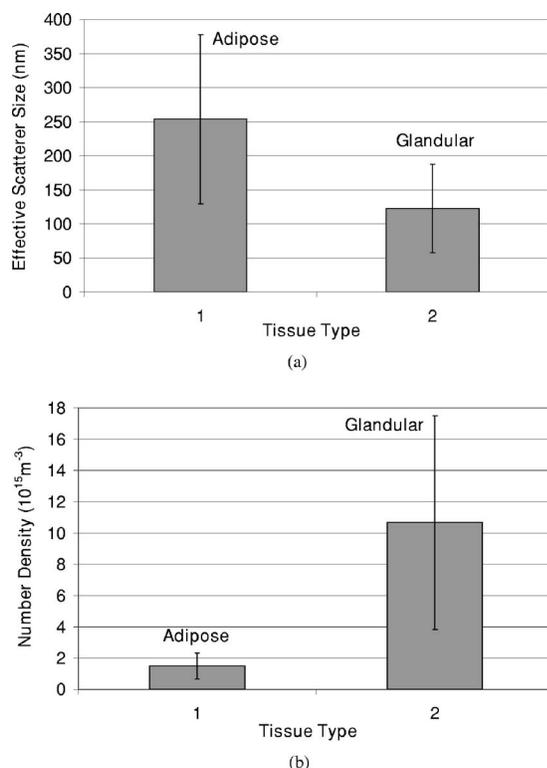
(a)

(b)

Fig. 8 The average tissue values are shown pooled for all MRI-NIR subject images, for effective scatterer size (a), and number density (b), for adipose and fibroglandular tissues.

used to estimate effective scatterer size first, and then effective number density can be readily determined. In making assumptions about the exponential shape of the histogram of scattering particle sizes, and in restricting the data to a sparse number of wavelengths, there is inherent neglect of any oscillatory spectral components that may be present. In addition, a further assumption was made that $n_1 = 1.36$ and $n_2 = 1.4$, for the refractive indexes with material 1 being cellular cytoplasm and fluid and material 2 being the bilipid membrane.

The Intralipid phantom study provided a reasonable way for image reconstruction of the effective scatterer size and number density, with a mean size value of 106 nm and standard deviation of 4 nm (as seen in Fig. 3). This result agrees to within 9% of the expected value of 97 ± 3 nm, suggesting that this method is accurate in this case.

In the patient study, for a cancer patient, the estimated effective scatterer sizes for tumor tissue and the background normal tissue were 535 nm and 603 nm. The estimated number density for tumor tissue and the background normal tissue were 12.4×10^{15} m^{-3} and 7.1×10^{15} m^{-3}, respectively. It indicated that for the cancer tissues examined here, they had smaller effective scatterer size and larger effective number density than the background normal tissue, on average. For the benign tumor patients, the estimated effective scatterer size for tumor and background normal tissue were 212 nm and 229 nm, respectively; the estimated effective number density for tumor and background normal tissue were 11.0 $\times 10^{15}$ m^{-3} and 10.9×10^{15} m^{-3}, respectively. For benign tu-

mors, there was not a significant difference between the tumor tissue and the background normal tissue.

For the MRI-NIR subject study, the estimated effective scatterer sizes for adipose and fibroglandular tissues were 254 nm and 123 nm, respectively. The estimated effective number density for adipose tissue and fibroglandular tissues were 1.5×10^{15} m^{-3} and 10.7×10^{15} m^{-3}, separately. This result indicated that the fibroglandular tissue had smaller effective scatterer size and larger effective number density than the adipose tissue, which agrees with the physiologically understood structure of adipose being larger lipid particles and fibroglandular being a compound of smaller intracellular and extracellular structures.

One of the larger differences in this study, which is different from earlier Mie scattering estimation studies, is the estimate that the distribution of the scattering particle sizes in breast tissue are exponentially weighted. This is not a common assumption in other papers, yet our preliminary work in electron microscopy verifies that this is indeed the case.[63] This is also in agreement with the Intralipid results by van Staveren et al.[25] Several other papers use a likelihood function[10] rather than a pure exponential one, which has the problem of requiring more free parameters for the shape of the function, making the calculations even more problematic. Yet, the sizes of particles nearest zero have the least impact upon the scattering spectrum, so the difference between a likelihood function and a pure exponential may be insignificant. Clearly, further analysis of this assumption should be undertaken, and electron microscopy studies to verify this have been completed and will be reported soon.

There are several ways potentially to improve the accuracy and precision of the effective scatterer size estimates reported here. The accuracy is likely to be increased by using a reduced scattering coefficient spectrum over a wider range in the spectrum and with more wavelengths. Simulation results indicate that the fitting algorithm improves with increased number of wavelengths; however, our current tomography system is limited to only six, although more will be added in the near future. Another approach to improve the estimate is to measure the scattering particle size histogram specifically by electronic microscopy, as was done explicitly for Intralipid in the paper by van Staveren et al.[25] and given particle size histograms could be applied to different tissues individually if the system is used in MRI-guided mode. Other approaches such as studying the angular scattering dependence of thin samples may lead to similar information about the effective scatterer size.[9,16] A more accurate measurement of the range of changes observed in the refractive index could be used to improve the estimation, as the refractive index change is clearly not just a single value, but is likely an entire range of values that may or may not be correlated with the range of particle sizes.

5 Conclusions

In summary, the patient results indicated that for a cancer tissue, there was a difference in average effective scatterer size and number density between the cancer and normal tissue and that cancer tissue has smaller effective scatterer size and larger effective number density. In benign tumor tissue, there is no significant difference from the background tissue. The

MRI-NIR subject study indicated that the fibroglandular tissue has smaller effective scatterer size and larger effective number density than the adipose tissue.

The method outlined in this paper provides a reasonable estimation of effective particle size and density for diffuse tomography applications where there are limited numbers of wavelengths. When there is an exponential distribution to the scattering particles in the smaller size ranges, Mie theory can be used as a first order approximation of these parameters. Medical acceptance of images of particle size and number density may be easier to gain acceptance than scattering amplitude and power, due to the inherently clearer physical meaning of the words.

References

1. B. W. Pogue, S. Jiang, X. Song, S. Srinivasan, H. Dehghani, K. D. Paulsen, T. D. Tosteson, C. Kogel, S. Soho, and S. Poplack, "Near-infrared scattering spectrum differences between benign and malignant breast tumors measured in vivo with diffuse tomography," OSA Biomedical Optics Topical Meetings, Technical Digest, p. ThB1. (2004).
2. B. J. Tromberg, N. Shah, R. Lanning, A. Cerussi, J. Espinoza, T. Pham, L. Svaasand, and J. Butler, "Non-invasive in vivo characterization of breast tumors using photon migration spectroscopy," *Neoplasia* **2**(1-2), 26–40 (2000).
3. A. E. Cerussi, D. Jakubowski, N. Shah, F. Bevilacqua, R. Lanning, A. J. Berger, D. Hsiang, J. Butler, R. F. Holcombe, and B. J. Tromberg, "Spectroscopy enhances the information content of optical mammography," *J. Biomed. Opt.* **7**(1), 60–71 (2002).
4. B. W. Pogue, T. O. McBride, C. Nwaigwe, U. L. Osterberg, J. F. Dunn, and K. D. Paulsen, "Near-infrared diffuse tomography with a priori MRI structural information: testing a hybrid image reconstruction methodology with functional imaging of the rat cranium," *Proc. SPIE* **3597**, 484–492 (1999).
5. R. Srinivasan and M. Singh, "Laser backscattering and transillumination imaging of human tissues and their equivalent phantoms," *IEEE Trans. Biomed. Eng.* **50**(6), 724–730 (2003).
6. R. Cubeddu, C. D'Andrea, A. Pifferi, P. Taroni, A. Torricelli, and G. Valentini, "Effects of the menstrual cycle on the red and near-infrared optical properties of the human breast," *Photochem. Photobiol.* **72**(3), 383–391 (2000).
7. S. Fantini, M. A. Francecshini, G. Gaida, E. Gratton, H. Jess, W. W. Mantulin, K. T. Moesta, P. M. Schlag, and M. Kaschke, "Frequency-domain optical mammography: edge effect corrections," *Med. Phys.* **23**, 149–157 (1996).
8. V. Ntziachristos, A. G. Yodh, M. D. Schnall, and B. Chance, "MRI-guided diffuse optical spectroscopy of malignant and benign breast lesions," *Neoplasia* **4**(4), 347–354 (2002).
9. J. R. Mourant, T. M. Johnson, and J. P. Freyer, "Characterizing mammalian cells and cell phantoms by polarized backscattering fiberoptic measurements," *Appl. Opt.* **40**(28), 5114–5123 (2001).
10. V. Backman, V. Gopal, M. Kalashnikov, K. Badizadegan, R. Gurjar, A. Wax, I. Georgakoudi, M. Mueller, C. W. Boone, R. R. Dasari, and M. S. Feld, "Measuring cellular structure at submicrometer scale with light scattering spectroscopy," *IEEE J. Sel. Top. Quantum Electron.* **7**(6), 887–893 (2001).
11. L. T. Perelman, V. Backman, M. Wallace, G. Zonios, R. Manoharan, A. Nusrat, S. Shields, M. Seiler, C. Lima, T. Hamano, I. Itzkan, J. Van Dam, J. M. Crawford, and M. S. Feld, "Observation of periodic fine structure in reflectance from biological tissue: a new technique for measuring nuclear size distribution," *Phys. Rev. Lett.* **80**(3), 627 (1998).
12. A. Wax, C. Yang, V. Backman, K. Badizadegan, C. W. Boone, R. R. Dasari, and M. S. Feld, "Cellular organization and substructure measured using angle-resolved low-coherence interferometry," *Biophys. J.* **82**, 2256–2264 (2002).
13. R. Graaff, J. G. Aarnoudse, J. R. Zijp, P. M. A. Sloot, F. F. M. de Mul, J. Greve, and M. H. Koelink, "Reduced light-scattering properties for mixtures of spherical particles: a simple approximation derived from Mie calculations," *Appl. Opt.* **31**(10), 1370–1376 (1992).
14. H. K. Roy, Y. Liu, R. K. Wali, Y. L. Kim, A. K. Kromine, M. J. Goldberg, and V. Backman, "Four-dimensional elastic light-scattering fingerprints as preneoplastic markers in the rat model of colon carcinogenesis," *Gastroenterology* **126**(4), 1071–1081 (2004).
15. I. J. Bigio, S. G. Bown, G. Briggs, C. Kelley, S. Lakhani, D. Pickard, P. M. Ripley, I. G. Rose, and C. Saunders, "Diagnosis of breast cancer using elastic-scattering spectroscopy: preliminary clinical results," *J. Biomed. Opt.* **5**(2), 221–228 (2000).
16. A. Wax, C. Yang, V. Backman, M. Kalashnikov, R. R. Dasari, and M. S. Feld, "Determination of particle size by using the angular distribution of backscattered light as measured with low-coherence interferometry," *J. Opt. Soc. Am. A* **19**(4), 737–744 (2002).
17. A. M. K. Nilsson, C. Sturesson, D. L. Liu, and S. Andersson-Engels, "Changes in spectral shape of tissue optical properties in conjunction with laser-induced thermotherapy," *Appl. Opt.* **37**(7), 1256–1272 (1998).
18. B. Gelebart, E. Tinet, J. M. Tualle, and S. Avrillier, "Phase function simulation in tissue phantoms: a fractal approach," *Pure Appl. Opt.* **5**(4), 377–388 (1996).
19. J. M. Schmitt and G. Kumar, "Optical scattering properties of soft tissue: a discrete particle model," *Appl. Opt.* **37**(13), 2788–2797 (1998).
20. R. K. Wang, "Modelling optical properties of soft tissue by fractal distribution of scatterers," *J. Mod. Opt.* **47**(1), 103–120 (2000).
21. X. Wang, B. W. Pogue, S. Jiang, X. Song, K. D. Paulsen, C. Kogel, S. P. Poplack, and W. A. Wells, "Approximation of Mie scattering parameters in near-infrared tomography of normal breast tissue in vivo," *J. Biomed. Opt.* **10**(5), 051704 (2005).
22. R. Drezek, A. Dunn, and R. Richards-Kortum, "Light scattering from cells: finite-difference time-domain simulations and goniometric measurements," *Appl. Opt.* **38**(16), 3651 (1999).
23. H. Liu, B. Beauvoit, M. Kimura, and B. Chance, "Dependence of tissue optical properties on solute-induced changes in refractive index and osmolarity," *J. Biomed. Opt.* **1**, 200–211 (1996).
24. B. Chance, Q. Luo, S. Nioka, D. C. Alsop, and J. A. Detre, "Optical investigations of physiology: a study of intrinsic and extrinsic biomedical contrast," *Philos. Trans. R. Soc. London, Ser. B* **352**, 707–716 (1997).
25. H. J. van Staveren, C. J. M. Moes, J. van Marle, S. A. Prahl, and M. J. C. van Gemert, "Light scattering in intralipid-10% in the wavelength range of 400–1100 nm," *Appl. Opt.* **30**(31), 4507–4514 (1991).
26. C. F. Borhen and D. R. Huffman, *Absorption and Scattering of Light by Small Particles*, John Wiley & Sons, Inc. (1998).
27. H. C. van de Hulst, *Light Scattering by Small Particles*, New York: Dover Publications, Inc. (1981).
28. V. Backman, R. Gurjar, L. T. Perelman, V. Gopal, M. Kalashnikov, K. Badizadegan, A. Wax, I. Georgakoudi, M. Mueller, C. W. Boone, I. Itzkan, R. R. Dasari, and M. S. Feld, "Imaging and measurement of cell structure and organization with submicron accuracy using light scattering spectroscopy," *Proc. SPIE* **4613**, 101–110 (2002).
29. J. R. Mourant, J. P. Freyer, A. H. Hielscher, A. A. Eick, D. Shen, and T. M. Johnson, "Mechanisms of light scattering from biological cells relevant to noninvasive optical-tissue diagnostics," *Appl. Opt.* **37**(16), 3586–3593 (1998).
30. H. B. Jiang, "Subcellular sizing with polarized light spectroscopy," *Opt. Commun.* **226**(1-6), 279–283 (2003).
31. A. H. Hielscher, J. R. Mourant, and I. J. Bigio, "Influence of particle size and concentration on the diffuse backscattering of polarized light from tissue phantoms and biological cell suspensions," *Appl. Opt.* **36**(1), 125–135 (1997).
32. A. Wax, C. Yang, M. G. Muller, R. Nines, C. W. Boone, V. E. Steele, G. D. Stoner, R. R. Dasari, and M. S. Feld, "In situ detection of neoplastic transformation and chemopreventive effects in rat esophagus epithelium using angle-resolved low-coherence interferometry," *Cancer Res.* **63**, 3556–3559 (2003).

33. H. B. Jiang, "Frequency-domain fluorescent diffusion tomography: a finite-element-based algorithm and simulations," *Appl. Opt.* **37**(22), 5337–5343 (1998).

34. H. B. Jiang, G. Marquez, and L. V. Wang, "Determination of particle size distribution in concentrated suspensions: Photon migration approach," *OSA Trends Opt. Photonics Ser.* **21**, 92 (1998).

35. B. J. Tromberg, O. Coquoz, J. B. Fishkin, T. Pham, E. R. Anderson, J. Butler, M. Cahn, J. D. Gross, V. Venugopalan, and D. Pham, "Non-invasive measurements of breast tissue optical properties using frequency-domain photon migration," *Philos. Trans. R. Soc. London, Ser. B* **352**, 661–668 (1997).

36. T. Durduran, R. Choe, J. P. Culver, L. Zubkov, M. J. Holboke, J. Giammarco, B. Chance, and A. G. Yodh, "Bulk optical properties of healthy female breast tissue," *Phys. Med. Biol.* **47**(16), 2847–2861 (2002).

37. B. W. Pogue, S. P. Poplack, T. O. McBride, W. A. Wells, K. S. Osterman, U. L. Osterberg, and K. D. Paulsen, "Quantitative hemoglobin tomography with diffuse near-infrared spectroscopy: Pilot results in the breast," *Radiology* **218**(1), 261–266 (2001).

38. S. P. Poplack, K. D. Paulsen, A. Hartov, P. M. Meaney, B. W. Pogue, A. N. Tosteson, M. R. Grove, S. K. Soho, and W. A. Wells, "Electromagnetic breast imaging: Average tissue property values in women with negative clinical findings," *Can. J. Neurol. Sci.* **231**, 571–580 (2004).

39. K. Blyschak, M. Simick, R. Jong, and L. Lilge, "Classification of breast tissue density by optical transillumination spectroscopy: optical and physiological effects governing predictive value," *Proc. SPIE* **5260**, 568–579 (2003).

40. S. Srinivasan, B. W. Pogue, S. Jiang, H. Dehghani, C. Kogel, S. Soho, J. G. Chambers, T. D. Tosteson, S. P. Poplack, and K. D. Paulsen, "Interpreting hemoglobin and water concentration, oxygen saturation, and scattering measured by near-infrared tomography of normal breast in vivo," *Proc. Natl. Acad. Sci. U.S.A.*, **100**(21), 12349–12354 (2003).

41. A. E. Cerussi, A. J. Berger, F. Bevilacqua, N. Shah, D. Jakubowski, J. Butler, R. F. Holcombe, and B. J. Tromberg, "Sources of absorption and scattering contrast for near-infrared optical mammography [comment]," *Acad. Radiol.* **8**(3), 211–218 (2001).

42. J. R. Mourant, T. Fuselier, J. Boyer, T. M. Johnson, and I. J. Bigio, "Predictions and measurements of scattering and absorption over broad wavelength ranges in tissue phantoms," *Appl. Opt.* **36**(4), 949–957 (1997).

43. F. Bevilacqua, A. J. Berger, A. E. Cerussi, D. Jakubowski, and B. J. Tromberg, "Broadband absorption spectroscopy in turbid media by combined frequency-domain and steady-state methods," *Appl. Opt.* **39**(34), 6498–6510 (2000).

44. S. Jiang, B. W. Pogue, T. O. McBride, M. M. Doyley, S. P. Poplack, and K. D. Paulsen, "Near-infrared breast tomography calibration with optoelastic tissue simulating phantoms," *J. Electron. Imaging* **12**(4), 613–620 (2003).

45. S. Srinivasan, B. W. Pogue, S. Jiang, H. Dehghani, and K. D. Paulsen, "Spectrally constrained chromophore and scattering NIR tomography improves quantification and robustness of reconstruction," *Appl. Opt.* **44**(10), 1858–1869 (2004).

46. S. Srinivasan, B. W. Pogue, B. Brooksby, S. Jiang, H. Dehghani, C. Kogel, W. A. Wells, S. P. Poplack, and K. D. Paulsen, "Near-infrared characterization of breast tumors in-vivo using spectrally-constrained reconstruction," *Technol. Cancer Res. Treat.* **4**, 513-526 (2005).

47. B. Brooksby, S. Srinivasan, S. Jiang, H. Dehghani, B. W. Pogue, K. D. Paulsen, J. Weaver, C. Kogel, and S. P. Poplack, "Spectral-prior information improves near-infrared diffuse tomography more than spatial-prior," *Opt. Lett.* **30**(15), 1968–1970 (2005).

48. B. Brooksby, S. Jiang, H. Dehghani, C. Kogel, M. Doyley, J. B. Weaver, S. P. Poplack, B. W. Pogue, and K. D. Paulsen, "Magnetic resonance-guided near-infrared tomography of the breast," *Rev. Sci. Instrum.* **75**(12), 5262-5270 (2004).

49. B. Brooksby, "Combined near-infrared tomography and MRI to improve breast tissue chromophore and scattering assessment," PhD thesis, Dartmouth College, Hanover, N.H. (2005).

50. B. Brooksby, S. Jiang, H. Dehghani, B. W. Pogue, K. D. Paulsen, J. B. Weaver, C. Kogel, and S. P. Poplack, "Combining near infrared tomography and magnetic resonance imaging to study in vivo breast tissue: implementation of a Laplacian-type regularization to incorporate MR structure," *J. Biomed. Opt.* **10**(5), 050504 (2005).

51. R. L. Barbour, H. L. Graber, J. Chang, S. S. Barbour, P. C. Koo, and R. Aronson, "MRI-guided optical tomography: prospects and computation for a new imaging method," *IEEE Comput. Sci. Eng.* **2**, 63–77 (1995).

52. A. Borsic, W. R. B. Lionheart, and C. N. McLeod, "Generation of anisotropic-smoothness regularization filters for EIT," *IEEE Trans. Med. Imaging* **21**, 579–588 (2002).

53. X. Intes, C. Maloux, M. Guven, T. Yazici, and B. Chance, "Diffuse optical tomography with physiological and spatial *a priori* constraints," *Phys. Med. Biol.* **49**, 155–163 (2004).

54. J. P. Kaipio, V. Kolehmainen, M. Vauhkonen, and E. Somersalo, "Construction of nonstandard smoothness priors," *Inverse Probl.* **15**, 713–729 (1999).

55. B. Kanmani and R. M. Vasu, "Diffuse optical tomography using intensity measurements and the *a priori* acquired regions of interest: theory and simulations," *Phys. Med. Biol.* **50**, 247–264 (2005).

56. A. Li, E. L. Miller, M. E. Kilmer, T. J. Brukilaccio, T. Chaves, J. Stott, Q. Zhang, T. Wu, M. Choriton, R. H. Moore, D. B. Kopans, and D. A. Boas, "Tomographic optical breast imaging guided by three-dimensional mammography," *Appl. Opt.* **42**, 5181–5190 (2003).

57. B. W. Pogue and K. D. Paulsen, "High resolution near infrared tomographic imaging simulations of rat cranium using *a priori* MRI structural information," *Opt. Lett.* **23**, 1716 (1998).

58. M. Schweiger and S. R. Arridge, "Optical tomographic reconstruction in a complex head model using *a priori* boundary information," *Phys. Med. Biol.* **44**, 2703–2721 (1999).

59. M. Vauhkonen, D. Vadasz, J. P. Kaipio, E. Somersalo, and P. A. Karjalainen, "Tikhonov regularization and prior information in electrical impedance tomography," *IEEE Trans. Med. Imaging* **17**, 285–293 (1998).

60. A. Amelink, M. P. L. Bard, S. A. Burgers, and H. J. C. M. Sterenborg, "Single-scattering spectroscopy for the endoscopic analysis of particle size in superficial layers of turbid media," *Appl. Opt.* **42**(19), 4095–4101 (2003).

61. B. Beauvoit, H. Liu, K. Kang, P. D. Kaplan, M. Miwa, and B. Chance, "Characterization of absorption and scattering properties for various yeast strains by time-resolved spectroscopy," *Cell Biophys.* **23**(1-3), 91–109 (1993).

62. B. Brooksby, S. Srinivasan, S. Jiang, H. Dehghani, B. W. Pogue, and K. D. Paulsen, "Spectral priors improve near-infrared diffuse tomography more than spatial priors," *Opt. Lett.* **30**(15), 1968–1970 (2005).

63. M. Bartek, X. Wang, W. A. Wells, K. D. Paulsen, and B. W. Pogue, "Estimation of subcellular particle size histograms with electron microscopy for prediction of optical scattering in breast tissue," *J. Biomed. Opt.* **11**, (2006) (in press).